A Modified PGA for Spaceborne SAR Scintillation Compensation Based on the Weighted Maximum Likelihood Estimator and Data Division

Hongcheng Zeng, *Member, IEEE*, Wei Yang, Pengbo Wang, and Jie Chen, *Senior Member, IEEE*

***Abstract*—The P-band spaceborne synthetic aperture radar (SAR) is significantly affected by ionospheric scintillation. Although the traditional phase gradient autofocus (PGA) can estimate and compensate for the scintillation phase of the single-polarization SAR data, the quality of the refocused image will degrade at the scene edge. In this article, a modified PGA based on the weighted maximum likelihood (WML) estimator and data division is proposed for full-scene image refocusing. First, a data division strategy for scintillation corrupted image is introduced, which is based on the prior scintillation information including its power spectral density and autocorrelation function. Then, some preprocessing steps including data selection, circular shifting, and windowing are performed for suppressing the noise and clutter. Finally, the scintillation phase is estimated by the WML estimator with fewer iterations, and after the scintillation phase of all data blocks is obtained, the distorted full-scene image is refocused. Using the generated wideband ionospheric scintillation model phase screen, numerical simulations based on point targets and scenes derived from real spaceborne SAR data are carried out. The evaluation results about resolution, peak side-lobe ratio, integral side-lobe ratio, correlation coefficient, and image entropy demonstrate the effectiveness of the proposed algorithm.**

***Index Terms*—Data division strategy, phase gradient autofocus (PGA), scintillation effect, synthetic aperture radar (SAR), weighted maximum likelihood (WML).**

I. Introduction

STATE-OF-THE-ART spaceborne synthetic aperture radar (SAR) satellites in orbit are capable of operating in S-, L-, C-, and X-bands [1]. As P-band allows penetration through soil and vegetation canopy, the P-band spaceborne SAR has been developing quickly in recent years, and one example is the planned launch of a P-band SAR satellite (BIOMASS) in 2022 by the European Space Agency, which will focus on forest biomass measurement [1]. Due to its long working wavelength, P-band spaceborne SAR will suffer from various ionospheric effects, including Faraday rotation (FR) [3], dispersion [4], and scintillation [5].

Manuscript received March 11, 2022; revised April 29, 2022; accepted May 11, 2022. Date of publication May 16, 2022; date of current version May 25, 2022. This work was supported by the National Natural Science Foundation of China under Grant 62101014. *(Corresponding author: Pengbo Wang.)*

The authors are with the School of Electronics and Information Engineering, Beihang University, Beijing 100191, China (e-mail: zenghongcheng@buaa.edu.cn; yangweigigi@sina.com; wangpb7966@buaa.edu.cn; chenjie@buaa.edu.cn).

Digital Object Identifier 10.1109/JSTARS.2022.3175263

FR is a magnetoionic effect and it transfers signal energy between polarizations [6]. Many estimators for FR correction have been proposed, such as Bickel and Bates estimator [7], Freeman's estimator [8], Chen and Quegan estimator [9], and so on [10]. The dispersion effect will introduce a frequency-dependent phase to the SAR range signal, which leads to range defocusing especially in high-resolution case [4], [11]. Normally, the contrast optimization autofocus method [12] or multilook registration autofocus [13] can compensate for the dispersion effectively. Different from the FR and dispersion effects, caused by small-scale ionospheric irregularities, the scintillation effect will induce random fluctuation phase error in the azimuth signal, leading to azimuth defocusing, azimuth shift and amplitude stripes in long-wavelength (P-band and L-band) spaceborne SAR images, and these distortions become stronger as the working frequency decreases [5], [14]–[16]. As the scintillation phase has randomly fluctuated, it is really difficult to get the mathematical expression of the scintillation phase in the SAR signal. Therefore, scintillation compensation is a crucial issue in long-wavelength spaceborne SAR imaging.

The state-of-the-art method for estimating and compensating for the SAR scintillation phase is the FR-based methodology, but fully polarized SAR data are required [5]. For single-polarization SAR, autofocus techniques are proposed for refocusing the image distorted by scintillation, such as phase gradient autofocus (PGA) [16]–[18] and the minimum-entropy method [19], [20]. PGA is a nonparametric autofocus method and mainly used in airborne SAR motion compensation. PGA-based algorithms are sensitive to the quality of initial input data, and a sample selection technique has been widely used [21]. Besides, PGA with data division is always performed for estimation and compensation of the spatial variation phase error [21], [22]. Based on the contrast measurement, quality PGA uses the high-quality sample data to achieve a faster convergence than the traditional PGA [22], which means that fewer iteration cycles are required. Weighted least-squares based PGA [24] and weighted maximum likelihood (WML) estimator [25] based PGA are proposed to minimize the residual phase error and improve its robustness. Since the scintillation effect will introduce random high-order phase errors, PGA based algorithms become a good tool for spaceborne SAR scintillation compensation.

However, the spatial variation effect of the scintillation phase is not considered in the traditional PGA-based scintillation compensation method [16], and the quality of the refocused image

This work is licensed under a Creative Commons Attribution 4.0 License. For more information, see https://creativecommons.org/licenses/by/4.0/

will decrease significantly at the scene edge. Data division is normally used for spatial-temporal irregularities defocused data and has shown good performance [22]. So, standard PGA with data division can be used for scintillation compensation on the whole scene. But, the tradition data division strategy is proposed for motion error compensation or whole scene SAR imaging [21], [22], and the available data division strategy is not suitable for scintillation corrupted image data. Besides, scintillation phase estimation by data blocks is time-consuming, especially in wide scene images. Moreover, much more iterations in traditional PGA will also affect the processing efficiency. Therefore, to estimate and compensate for the scintillation phase efficiently, fewer iterations, and suitable data division strategy are necessary. In this article, motivated by the advantages of data division and WML estimator, a modified PGA is proposed for full-scene scintillation-distorted spaceborne SAR image refocusing.

The rest of this article is organized as follows. The background of scintillation and its simulation in SAR is presented in Section II, and details of the proposed modified PGA are provided in Section III. In Section IV, simulations are carried out to validate the effectiveness of the proposed algorithm, and conclusions are drawn in Section V.

II. Ionospheric Scintillation and its Simulation in SAR

As the real spaceborne P-band data are unavailable, the scintillation phase and scintillation distorted image simulation are very important. Besides, using scintillation simulated data is helpful to evaluate the performance of the scintillation correction method. So, the scintillation phase screen and its simulation in SAR will be presented in this section.

A. Scintillation and Phase Screen

Total electron content (TEC) varies on spatial scales extending from a few meters to thousands of kilometers. The large-scale structure of the ionosphere leads to dispersion. There are also structures within ionosphere on scales significantly less than the synthetic aperture, commonly referred to as irregularities. Those spatial-temporal irregularities in the electron density of the ionosphere will lead to scattering of the SAR waveform, and introduce phase fluctuations, called the scintillation effect. For scintillation, the phase delay variations across the synthetic aperture are proportional to TEC variations, and can be obtained from the TEC map, using [16]

$$\varphi_{\text{SCIN}} = \frac{4\pi\varsigma}{cf_0}\text{TEC} \tag{1}$$

where $\varsigma = e^2/8\pi^2\varepsilon_0 m_e = 40.3082\text{m}^3/\text{s}^2$, TEC is the total electron content in the unit of TECU, c is the speed of light, and f_0 is the carrier frequency. As shown in (1), spatial-temporal irregularities in the electron density of the ionosphere will cause perturbations in the echo signal phase delay, which in turn lead to SAR image distortion, including defocusing, spatial azimuth shifts, and interferometric coherence reduction.

The scintillation effect is a random process and is often found to have a power law scale-size spectrum [5], [26]. To make stochastic processing feasible, the phase screen theory is introduced, which assumes that the vertical effects can be integrated to form a phase screen, a two-dimensional (2-D) surface at a nominal constant height. The wideband ionospheric scintillation model (WBMOD) from NorthWest Research Associates [27] is widely used in scintillation simulation. To generate the phase screen, the following information is needed: basic information about satellite orbit and SAR parameters, planetary disturbance index (K_p), Zurich sunspot number (R_z), and confidence interval (CI) for C_kL. Two simulated phase screens using power law spectra derived from the WBMOD are presented in Fig. 1, with 30° looking angle, 98° inclination angle, 100 MHz signal bandwidth, a sun-synchronous orbit with local ascending time at 06:00, and a scene center at a boreal location (60°N, 110°W). As the scintillation phase is a random process, the actual scintillation phase simulation realizations depend on the random seed used in the simulation. So, even the scintillation parameters are same, the structure of the scintillation disturbance is totally different in its details under the condition of different seeds. The strong case of the simulated phase screen (C_kL CI $= 90\%$, $R_z = 62.8$, $K_p = 7$) is presented in Fig. 1(a), whereas the medium case (C_kL CI $= 90\%$, $R_z = 62.8$, $K_p = 3$) in Fig. 1(b). It should be noted that the background ionosphere is set to zero, as only scintillation effect is of concern in this article. Then, based on the generated scintillation phase screen, the scintillation effect can be simulated in SAR, which will be presented in Section II-B.

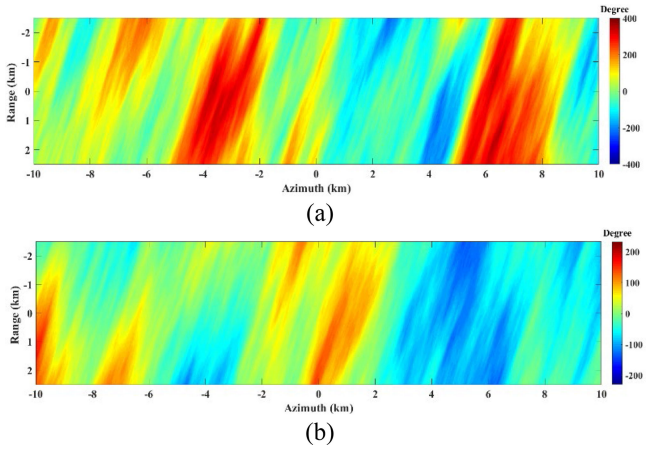

Fig. 1. Phase screens generated by WBMOD. (a) Strong. (b) Medium.

As the autocorrelation function (ACF) can be used to characterize the inherent correlation of the random scintillation phase, the ACF and its 2-D profile for the strong scintillation case are presented in Fig. 2. As shown, the fluctuation phase caused by scintillation changes sharply along with both range and azimuth directions and the variation of the scintillation phase along each direction is also different. For example, the width of the strong scintillation in Fig. 1(a) is about 3 km when the peak energy of the azimuth profile of ACF decreases by 3 dB, which is twice the width in the range direction. Therefore, the spatial variation of scintillation should be considered, if the PGA methods are used for scintillation compensation. Besides, according to the Wiener–Khinchin theorem, the power spectral density (PSD) of

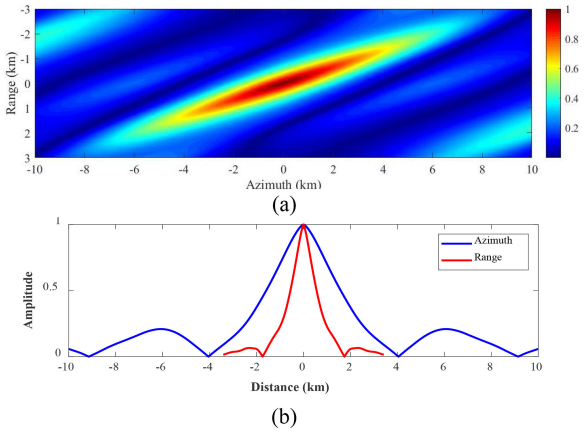

Fig. 2. ACF of the strong scintillation in Fig. 1(a). (a) 2-D ACF. (b) Azimuth and range profile of this ACF.

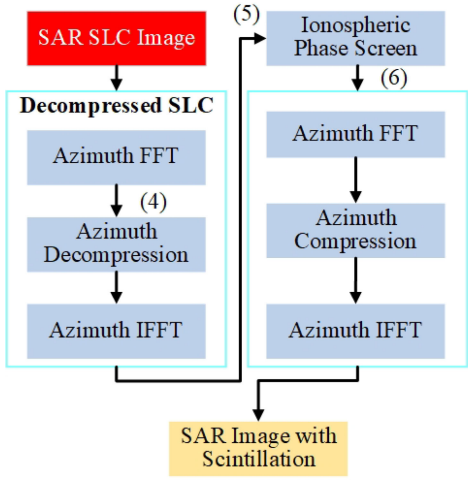

Fig. 3. Processing flow of the scintillation simulation in SAR.

a stationary random process is the Fourier transform of its ACF. Based on Riono's form, the PSD of the scintillation phase can be modeled by [12], [14]

$$\mathrm{PSD}\left(\kappa\right) = T'\left(\sqrt{\kappa_0^2 + \kappa^2}\right)^{-p} \tag{2}$$

where κ is the spatial scale wavenumber, κ_0 is the outer scale wavenumber, p is the power law index, and T' is decided by the classical electron radius, wavelength, geometric factor, look angle and the integrated strength of ionospheric turbulence. Hence, the ACF of the scintillation phase can also be obtained based on the PSD form in (2).

B. Scintillation Simulation in SAR

To assess the distortions of the scintillation effect and the performance of the scintillation correction method, using well-characterized simulated scintillation SAR image is very important. In this section, scintillation simulation in a scintillation-free SAR single-look complex (SLC) image is presently based on the phase screen theory, and its processing flow is shown in Fig. 3.

As shown in Fig. 3, the scintillation-free SAR SLC image should be refocused at the height of the phase screen first and obtained as a decompressed SLC image. The processing detail is as follows:

$$S_{\mathrm{iono}} = \mathrm{IFFT}_A\left[\mathrm{FFT}_A\left(S_{\mathrm{slc}}\right) \cdot \exp\left\{j\phi\left(f_a, R_{\mathrm{iono}}\right)\right\}\right] \tag{3}$$

where S_{slc} is the focused SAR image, S_{iono} is the refocused data at the height of phase screen, $\mathrm{FFT}_A(\cdot)$ is the Fourier transform along the azimuth direction, $\mathrm{IFFT}_A(\cdot)$ is the inverse Fourier transform, and the decompression function $\phi(f_a, R_{\mathrm{iono}})$ is given by [5]

$$\phi\left(f_a, R_{\mathrm{iono}}\right) = \frac{4\pi}{\lambda}\left(R_{\mathrm{ref}} - R_{\mathrm{iono}}\right)\left(\sqrt{1 - \left(\frac{f_a\lambda}{2v}\right)^2} - 1\right) \tag{4}$$

where R_{ref} is the reference range, R_{iono} the range to the phase screen, f_a the azimuth frequency, λ the signal wavelength, and v the satellite velocity. Once the SAR image is refocused at the phase screen, the simulated phase screen can be added directly by multiplying the scintillation phase, given by

$$S_{\mathrm{ph}} = S_{\mathrm{iono}} \cdot \exp\left\{j\varphi_{\mathrm{scin}}\right\} \tag{5}$$

where S_{ph} is the distortion image, and φ_{scin} is the 2-D phase screen which is based on a power law irregularity spectrum derived from the WBMOD model. Finally, the focusing plane of SAR is reversed from the phase screen layer to the ground level, and the final SAR image S_{dis} with scintillation is

$$S_{\mathrm{dis}} = \mathrm{IFFT}_A\left[\mathrm{FFT}_A\left(S_{\mathrm{ph}}\right) \cdot \exp\left\{-j\phi\left(f_a, R_{\mathrm{iono}}\right)\right\}\right]. \tag{6}$$

Therefore, the distortions introduced by ionospheric scintillation are simulated by the superposition of a phase screen at a given effective height between the scene and orbit path.

III. Modified PGA Algorithm Based on WML and Data Division

The PGA is based phase error redundancy. However, due to spatial variation of the scintillation phase, the traditional PGA is really difficult to estimate the scintillation phase precisely at the edge of the SAR imaging scene. Considering phase fluctuation, 2-D block processing is recommended, but it will seriously affect the processing efficiency. In addition, iterations in PGA are time-consuming as multiple repeated processing steps are involved. Therefore, it is crucial to propose an efficient modified PGA algorithm for scintillation estimation and compensation in spaceborne SAR.

A. Traditional PGA for Scintillation Compensation

The original PGA was proposed for airborne spotlight SAR image focusing, and PGA and its improved version have been widely used for motion compensation or high-order phase errors compensation. By modifying the standard PGA, it can be suitable for scintillation phase estimation. The processing flow is presented in Fig. 4, and the key steps are summarized as follows [8]. First, windowing and circular shifting are performed to remove the linear phase and enhance the signal to clutter

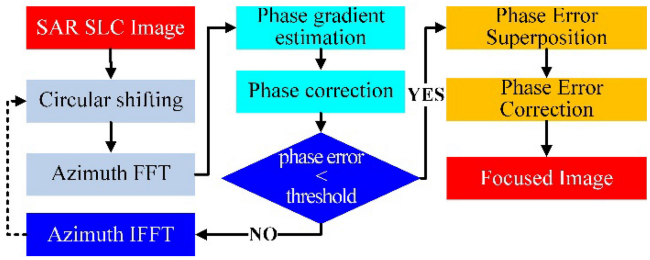

Fig. 4. Processing flow of the traditional PGA.

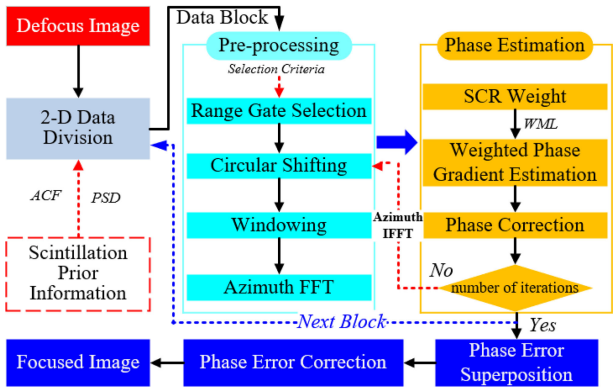

Fig. 5. Illustration of the proposed modified PGA algorithm.

ratio (SCR) of the selected range gates. Then, phase gradient estimation is performed based on the linear unbiased minimum variance estimator, given by

$$\dot{\phi}(n) = \frac{\sum_{k=0} \mathrm{Im}\left[\dot{S}_k(n) \cdot \mathrm{conj}\left[S_k(n)\right]\right]}{\sum_{k=0} |S_k(n)|^2} \tag{7}$$

where $\dot{\phi}(n)$ denotes the gradient of the phase error, $\underline{S_k}(n)$ is the Doppler-domain signal in the kth range gate, $\dot{S}_k(n)$denotes its gradient, conj$(\cdot)$ is the conjugated function, and Im$(\cdot)$ is the operation taking the imaginary part. Next, phase correction is performed with the estimated phase $\hat{\phi}(n)$, which is the integration of the phase gradient $\dot{\phi}(n)$. Finally, all above-mentioned processing steps are repeated, as iteration is necessary for conventional PGA.

B. Modified PGA

As analyzed in Section II.A, the spatial variation of scintillation should be considered. In tradition, PGA with data division can be used to compensate for the spatial variation phase error [22]. So, the data division is first introduced into the modified PGA to compensate for the spatial variation of the scintillation phase. Here, the strategy of the data division is important, which will directly affect the efficiency of the PGA. Besides, the number of iterations will also affect its efficiency. To improve the efficiency and performance of the modified PGA, the following ideas are considered:

1) divide the image data into multiple blocks;
2) a criterion for range gate selection, as poor-quality data will degrade the estimation and too much range gates will degrade the estimation efficiency;
3) reduce the number of iterations.

Therefore, motivated by the advantages of data division and WML estimator, a modified PGA algorithm is proposed in the following, where data division is performed for spatial variation phase compensation and WML estimator is performed for improving convergence speed. As shown in Fig. 5, the modified PGA including four stages: 2-D data division, preprocessing, phase estimation, and scintillation correction.

1) 2-D data division: The first stage is image 2-D data division to reduce the influence of spatial variation of the scintillation phase in PGA processing. Different from the existing data division strategy, the scintillation phase has randomly fluctuated. As known, the PSD or ACF can be used to describe the fluctuation of the random phase. So, we divide the image data in a new manner in this article, as the block length is dependent on the ACF of scintillation phase. Normally, the ACF is not known before estimation. However, based on research on scintillation, the PSD of phase screen can be modeled in Rino's form [14], given some prior information such as signal wavelength, phase spectral index, turbulence outer scale, and so on. So, all phase screens have the same ACF structure if the scintillation parameters are same. Then, the ACF can be obtained by the scintillation PSD information through their Fourier transform relationship. By setting the threshold for ACF peak energy reduction, such as 3 dB, the width of each divided block in azimuth and range directions can be decided. For example, as shown in Fig. 2, the width of azimuth profile of the ACF is about 3 km, and about 1.5 km for the range profile, using the 3-dB threshold. Thus, in this case, the image data can be divided into multiple blocks with an area of 3 km $\times$ 1.5 km. Since the scintillation phase in medium and weak phase screen cases changes slowly, the number of data blocks will be greatly reduced.

Therefore, this new data division strategy can be used in PGA processing, and it should be decided before the scintillation phase compensation. In practice, the PSD of ionospheric scintillation can be obtained based on the local forecast information of the ionosphere.

2) Preprocessing: The preprocessing stage is implemented for suppressing the influence of noise and clutter. Based on the selection criterion (high average power [16] or Q_k in [21]), sample selection is first performed, which will significantly reduce the processing time and improve the efficiency of the phase estimation. In the next, circular shifting is performed for shifting the strongest scatter to the azimuth center time and removing the linear phase of the scintillation phase. Then, windowing is adopted to further suppress the influence of noise and clutter signal on PGA estimation kernel. Usually, a center-symmetric window function with a varying window size is used. In the first iteration of phase estimation, a large window size is usually employed to try to capture the complete scintillation phase error, and the following iterations will work on a smaller window size. Finally, azimuth fast Fourier transform is applied to transform the data into the azimuth frequency domain.

3) Phase estimation: Phase estimation is the core of the proposed method. In traditional PGA, tens of iterations are needed and the convergence speed is very slow. As presented in [25], the WML estimator has a nice performance on phase error estimation and convergence speed. So, the WML estimator is introduced into the modified PGA. By SCR weighting, the WML estimator can significantly enhance the contribution of high-quality data and reduce the interference of low SCR data. Using the WML estimator, high precision phase error estimation can be achieved by several iterations or just one iteration for a slowly varying phase for an even lower computation load. In detail, first, the normalized SCR weights can be calculated by [23]

$$w_k = \frac{w'_k}{\sum_{k=0}^{K-1} w'_k}, \quad \frac{1}{w'_k} = \frac{1}{2\cdot \mathrm{SCR}_k} + \frac{5}{24\cdot (\mathrm{SCR}_k)^2} \tag{8}$$

where K is the number of range gates, and SCR_k is the SCR of the kth range gate given by

$$\mathrm{SCR}_k = \frac{d_k}{4\left(2{c_k}^2 - d_k\right) - 4c_k\sqrt{4{c_k}^2 - 3d_k}} \tag{9}$$

where

$$c_k = \frac{1}{N_a}\sum_{n=0}^{N_a-1} |S_k(n)|, \quad d_k = \frac{1}{N_a}\sum_{n=0}^{N_a-1} |S_k(n)|^2$$

and N_a is the azimuth sample number. Then, the WML estimation result is given by [24]

$$\hat{\phi}_{\mathrm{WML}}(n) = \arg \sum_{k=0}^{K-1} w_k \cdot [\mathrm{conj}\,[S_k(n)] \cdot S_k(n+1)] \tag{10}$$

where arg(·) represents the angle of a complex number. Then, the scintillation phase can be compensated using the estimated $\hat{\phi}_{\mathrm{WML}}(n)$. For the next iteration, azimuth IFFT is performed first, and then the processing flow starts with circular shifting with the new compensated data.

4) Scintillation correction: After all iterative processing of all blocks of data is completed, the scintillation phase screen is obtained by superposing the estimated phase error of each iteration, the scintillation phase error is then compensated accordingly and the finely refocused full-scene image is obtained by IFFT at the end.

IV. Experimental Results and Performance Analysis

In this section, numerical simulations are carried out to demonstrate the performance of the modified PGA algorithm for long-wavelength spaceborne SAR, using first simulated data for point targets, and then real spaceborne data corrupted by the simulated scintillation effect. Using well-characterized simulated data, the scintillation effect and the performance of the proposed algorithm can be accurately evaluated by resolution, peak side-lobe ratio (PSLR), integral side-lobe ratio (ISLR), correlation coefficient, and image entropy.

TABLE I
List of Simulation Parameters for Point Targets

Quantity	Value	Quantity	Value
Wavelength	0.6 m	Number of Iterations	2~3
Looking Angle	30°	Contrast Measure Q_k [21]	0.35
Signal Bandwidth	100 MHz	Satellite Height	600 km
Sampling Rate	120 MHz	Azimuth Resolution	3.5 m
Image Scene	4 km × 4 km	Point Targets	5 × 5

TABLE II
Imaging Quality Analysis in Strong and Medium Scintillation Cases

		Strong Scintillation			Medium Scintillation		
		ρ_a (m)	*PSLR* (dB)	*ISLR* (dB)	ρ_a (m)	*PSLR* (dB)	*ISLR* (dB)
A	Ideal	3.50	-23.46	-18.28	3.50	-23.46	-18.28
	Scintillation	4.16	-6.67	-2.36	3.55	-9.14	-7.33
	PGA	3.87	-8.35	-3.18	3.50	-14.61	-10.12
	Modified PGA	3.50	-22.75	-19.38	3.50	-23.33	-18.23
B	Ideal	3.50	-23.44	-18.27	3.50	-23.44	-18.27
	Scintillation	4.16	-6.57	-2.19	3.56	-9.56	-7.97
	PGA	3.52	-23.39	-18.14	3.50	-23.48	-18.28
	Modified PGA	3.50	-23.60	-18.20	3.50	-23.50	-18.30
C	Ideal	3.50	-23.46	-18.28	3.50	-23.46	-18.28
	Scintillation	4.17	-5.73	-1.61	3.52	-10.59	-8.65
	PGA	3.89	-7.55	-3.45	3.50	-15.49	-10.11
	Modified PGA	3.50	-23.37	-18.29	3.50	-23.11	-18.25

A. Results Using Simulated Point Targets

The effectiveness of the proposed algorithm is demonstrated first, with the listed parameters in Table I and simulated scintillation phase screen in Fig. 1. Considering the effect of strong scintillation in Fig. 1(a), the distorted image and its refocused version are presented in Fig. 6. As shown, the point targets are totally defocused along azimuth due to the scintillation effect, whereas all targets are refocused correctly after compensation. Here, based on the analysis in Sections II and III, the image data is divided into six blocks (two blocks in azimuth and three blocks in range). It should be noted that the number of iterations in traditional PGA is 20, but in the proposed PGA is 2∼3. So, the processing efficiency of the proposed modified PGA algorithm is better.

Moreover, azimuth profiles of the center target B with scintillation free (red line), distorted by medium scintillation or strong scintillation (blue line), and its refocused result (black line) are presented in Fig. 7. In the medium case, the sidelobes change significantly but the main lobe is almost unchanged, as the small random phase mainly degrades PSLR and ISLR, but not resolution [16]. However, the azimuth signal is defocused as the scintillation phase fluctuates violently in the strong case,

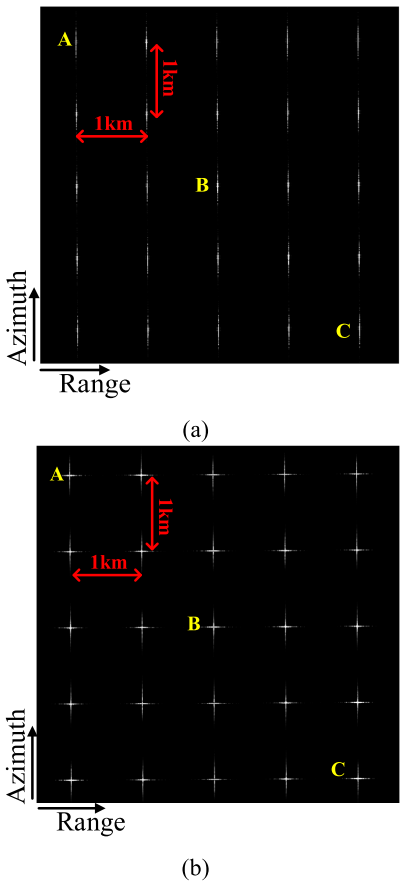

Fig. 6. Imaging results of point targets with strong scintillation. (a) Image with scintillation. (b) Compensation result by the proposed algorithm.

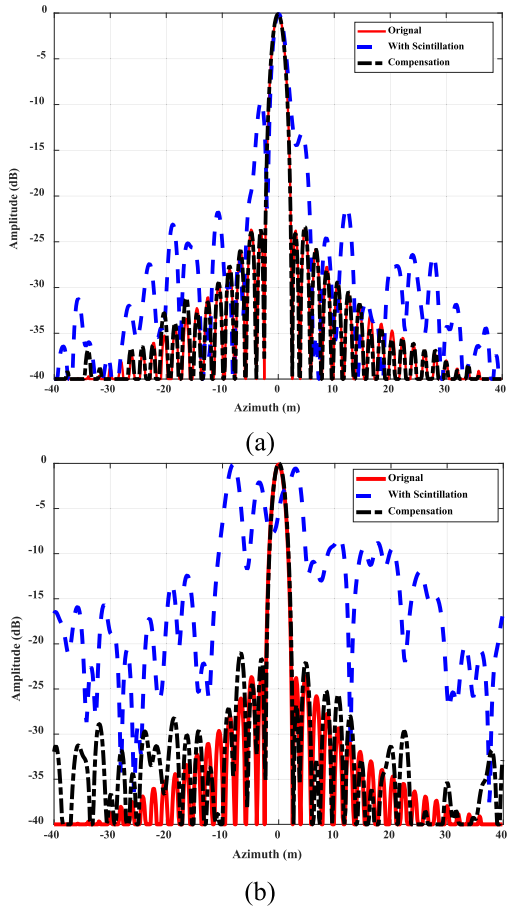

Fig. 7. Azimuth interpolation profile of target B. (a) Medium scintillation case. (b) Strong scintillation case.

which is consistent with the analysis in [16]. Besides, as shown in Fig. 7, the azimuth signal is refocused well by the proposed algorithm in both medium and strong cases. But the residual phase error after PGA in the strong case is a little larger, and the residual phase error is random, which mainly affects the sidelobes.

For comparison, the refocused imaging results of targets A, B, and C by the traditional PGA and the proposed one are presented in Fig. 8. As shown by the contour plot, all point targets are refocused by our proposed algorithm, and the center target B can be refocused as well using the traditional PGA. However, the phase error redundancy is invalid in scintillation, and the residual phase error after traditional PGA becomes large at the edge of the scene. Thus, targets A and B cannot be refocused accurately by the traditional PGA. Moreover, the azimuth resolution, PSLR, and ISLR for each target with scintillation-free, scintillation, compensated by PGA, and compensated by the proposed algorithm are listed in Table II. All these indicate a quality imaging result by our proposed algorithm, which has adapted to the full-scene requirement effectively.

B. Simulated Scintillation Effect With Spaceborne Real Data

Based on the real spaceborne SAR data (TerraSAR and ALOS-2), which is degraded by the simulated scintillation phase, experiments are carried out to examine the effectiveness of the proposed modified PGA. In the following, P-band and L-band image distortions due to scintillation are presented and the compensation results using traditional PGA and proposed modified PGA are presented.

First, P-band distorted SAR image compensation experiment on the city area scene is carried out based on TerraSAR data (ID: TSX1_SAR_20120717T225339). Although the spaceborne P-band data are unavailable, the scintillation corrupted SAR scenario data in P-band can be simulated using the method shown in Fig. 3, with the listed P-band parameters in Table I and simulated strong scintillation phase in the condition of P-band in Fig. 1(a). Here, without considering the different scattering characteristics in different signal bands, we can assume this simulated scintillation distorted data as the result of P-band data. The original data has a size of 3000 $\times$ 3000 pixels, with a pixel spacing of 1.9 m in azimuth and 0.9 m in ground range. The distorted image affected by the strong scintillation is presented in Fig. 9(a), and as shown, the image is totally defocused in azimuth. Then, the traditional PGA with no data division and the proposed one are applied to the distorted image, and the refocused images are presented in Fig. 9(b) and (c). In the proposed algorithm, the image data is divided into four blocks (two blocks in azimuth and two blocks in range), and the contrast measure Q_k is 0.4. As

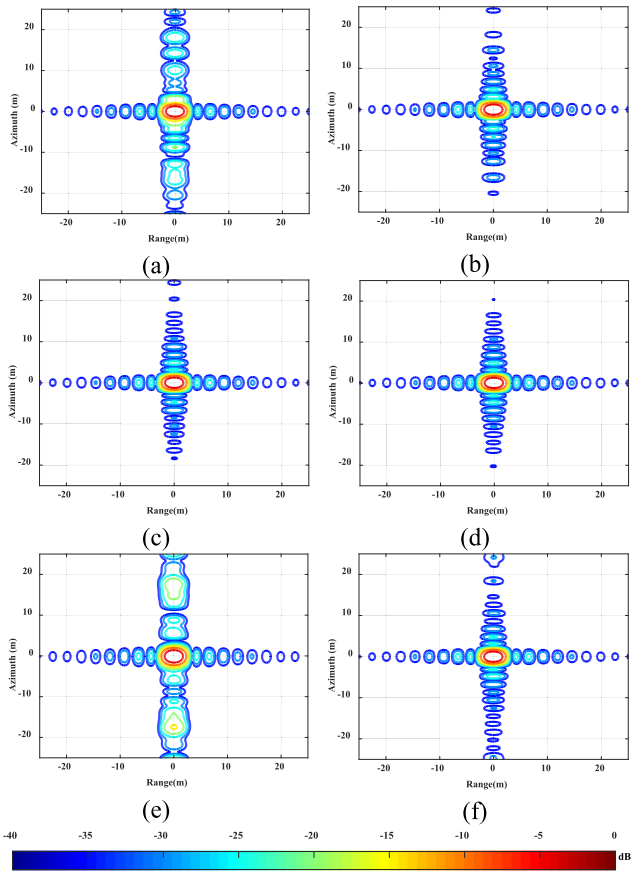

Fig. 8. Autofocusing results of target A/B/C. (a), (c), and (e) Contour plots of target A/B/C with traditional PGA. (b), (d), and (f) Contour plots of target A/B/C with the proposed modified PGA.

the enlarged images in Fig. 9 shown, the images after traditional PGA compensation are refocused, but the quality of the image processed by the modified algorithm is much better, and the side lobe of the strong target in this image is not obvious. The main reason is that the proposed algorithm considers the effect of the spatial scintillation phase, and its residual random phase error is much smaller than the traditional PGA, which mainly leads to increased sidelobes. Besides, the azimuth of a strong target in this image is also presented in Fig. 9(d), and as the blue line shows, the target is totally defocused due to strong scintillation, and it can be refocused by those two algorithms. But the sidelobes in traditional PGA (black line) are much higher than those in the proposed one (green line), which seriously corrupts the image quality.

Moreover, L-band distorted SAR image compensation experiment on Amazon rainforest is also carried out based on HH polarization PALSAR-2 data (ID: ALOS2011247000-140808-HBQR1). In this experiment, it is assumed that the PALSAR-2 data is scintillation-free, and a simulated extremely strong scintillation phase screen in L-band is introduced into the real PALSAR-2 data. As shown in Fig. 10, the scintillation phase in L-band is much smaller than that in P-band, as the scintillation phase is proportional to the signal wavelength. The original

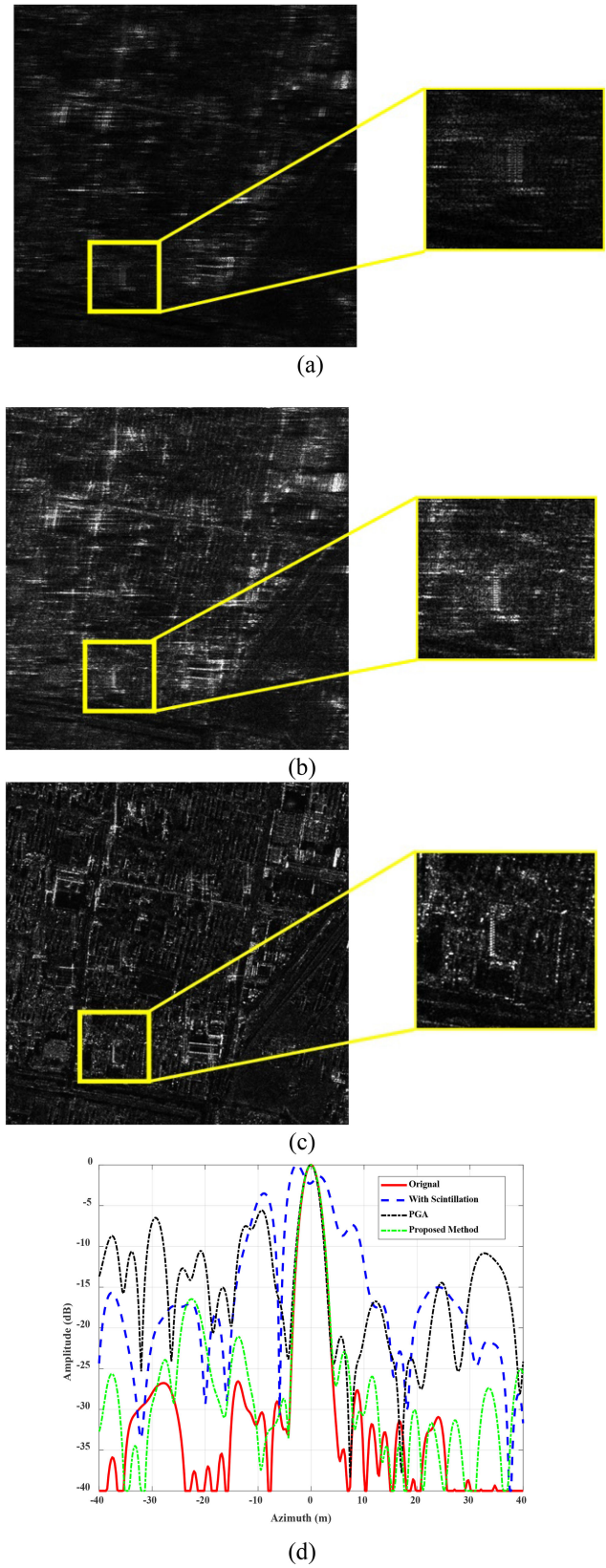

Fig. 9. Experimental results of real city area scenario. (a) Distorted image with strong scintillation. (b) Refocused image with traditional PGA. (c) Refocused image with the proposed algorithm. (d) Azimuth profile of a strong target in this image.

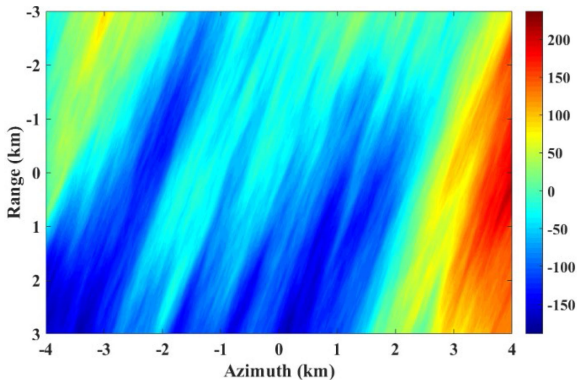

Fig. 10. Generated phase screen in L-band (simulation parameters: $C_k L$ CI = 90%, $R_z = 142.1$, $K_p = 7$).

data has a size of 3000 × 3000 pixels, with pixel spacing of about 3m in both sides, and a point-like target exists in this image area. Based on the ACF of the simulated scintillation phase screen, the image data is divided into six blocks (three blocks in azimuth and two blocks in range), and other PGA parameters setting are the same as the first experiment. Then, the experimental results about the distorted image, refocused image with traditional PGA, and refocused image with the proposed algorithm are presented in Fig. 11, and the interpolation contour map of this point-like target is also presented in each image result. As shown in Fig. 11(a), the scintillation will affect the azimuth focusing and the target may totally defocus in a strong scintillation case, even in L-band. Although the azimuth signal is trying to refocus by the traditional PGA, the residual phase error caused by the scintillation effect is still large, and as shown in Fig. 11(b), the point-like target is still defocused in azimuth in this strong scintillation case. For the proposed modified PGA, the spatial scintillation phase can be compensated considering the ACF of scintillation as the data division strategy. So, as shown in Fig. 11(c), the distorted image is refocused well, and enlarged image and the interpolation contour result show that the target is focused into a point-like target.

Moreover, as mentioned in [16] and [28], better focusing results in a smaller entropy and a larger correlation coefficient. So, the index of mean and deviation values of correlation coefficient [5] and image entropy [20], [28] are evaluated using the original scintillation-free image, distorted image and refocused images of those above-mentioned experiments. Here, the definition of correlation coefficient γ between two SLC SAR images S_1 and S_2 is

$$\gamma = \frac{|\langle S_1^* \cdot S_2 \rangle|}{\sqrt{\langle S_1 \cdot S_1^* \rangle}\sqrt{\langle S_2 \cdot S_2^* \rangle}} \tag{11}$$

where $\langle \cdot \rangle$ is the mean over a region of the image. Based on the definition, the correlation result between the original image and compensated images after traditional PGA and modified PGA are shown in Fig. 12. As shown in Fig. 12(b), most areas of this image become more correlated, which demonstrates the effectiveness of the proposed modified PGA.

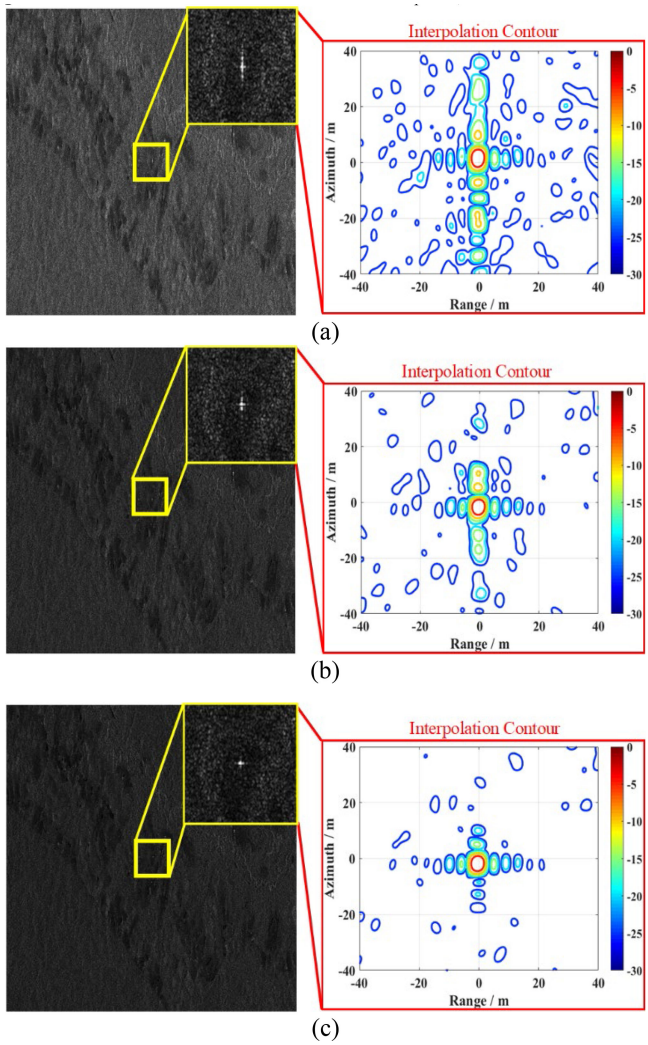

Fig. 11. Experimental results of rainforest scenario with PALSAR-2 data. (a) Distorted image with strong scintillation. (b) Refocused image with traditional PGA. (c) Refocused image with the proposed algorithm.

Besides, the definition of image entropy ε is

$$\varepsilon = \sum_i \sum_j \frac{|S(i,j)|^2}{\sum_i \sum_j |S(i,j)|^2} \ln \frac{\sum_i \sum_j |S(i,j)|^2}{|S(i,j)|^2} \tag{12}$$

where $S(i, j)$ denotes the element in the ith row and the jth column of the image.

Then, the evaluation results based on the correlation coefficient and image entropy based on those two experimental results are listed in Table III. As listed, the reduction of image entropy and the increase of correlation coefficient both indicate improvement of image quality by the proposed modified PGA. Therefore, the proposed modified PGA can refocus the scintillation distorted full-scene long-wavelength (P-band and L-band) spaceborne SAR image, and it has greater visual experience and evaluation index, compared with the tradition PGA.

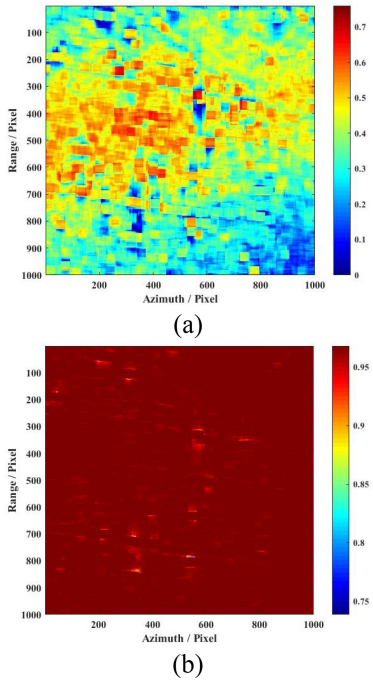

Fig. 12. Correlation coefficient results based on the first experiment data. (a) Correlation between original and traditional PGA. (b) Correlation between original and modified PGA.

TABLE III
EVALUATION RESULTS

		Entropy	Mean CorCoe [1]	Deviation CorCoe [1]
TerraSAR data	Original Image	10.22	--	--
	Distorted Image	11.70	0.28	0.09
	PGA	11.41	0.50	0.11
	Modified PGA	10.30	0.86	0.01
ALOS-2 data	Original Image	14.64	--	--
	Distorted Image	14.79	0.38	0.06
	PGA	14.68	0.64	0.04
	Modified PGA	14.65	0.96	0.01

[1]CorCoe: correlation coefficient between the original and distorted or refocused images.

V. CONCLUSION

Considering the 2-D spatial variation characteristics of scintillation phase, a modified PGA algorithm for scintillation compensation in spaceborne SAR has been proposed in this article, which borrows the idea of 2-D data division and WML estimator. In this article, motivated by the data division, the 2-D data division is introduced in the modified PGA, which makes the compensation of the spatial variation of the scintillation phase possible. Besides, a new data block division strategy is introduced according to the prior scintillation information about the PSD and ACF, and the length of each data block is the length that the peak energy of ACF decreases by a threshold, such as 3 dB. Therefore, in the proposed modified PGA, data division based on the introduced strategy is performed first. Then, some preprocessing steps including data selection, circular shifting and windowing are performed to suppress noise and clutter. In the next, the WML estimator is introduced for scintillation phase estimation, which can achieve near-convergence focusing with only a few or just one iteration and improve the efficiency of the modified PGA. At last, the scintillation phase screen is obtained and the distorted full-scene image is finely refocused. As demonstrated by numerical simulations of points targets and real scene with WBMOD phase screen, the proposed algorithm has a good performance on full-scene image refocusing.

Compared with the traditional PGA for scintillation compensation, the proposed modified PGA can refocus the scintillation corrupted image more effectively, considering the new data division strategy and WML estimator. Moreover, unlike the FR-based methodology, the proposed algorithm also provides a robust solution for refocusing a single polarimetric SAR scintillation distorted image. Our future work will focus on measuring of scintillation phase screen based on sub-aperture processing and PGA.

ACKNOWLEDGMENT

The authors would like to thank Prof. Shaun Quegan of the University of Sheffield, for providing the scintillation phase screens generated by the WBMOD.

REFERENCES

[1] A. Moreira, P. Prats-Iraola, M. Younis, G. Krieger, I. Hajnsek, and K. P. Papathanassiou, "A tutorial on synthetic aperture radar," *IEEE Geosci. Remote Sens. Mag.*, vol. 1, no. 1, pp. 6–43, Mar. 2013.

[2] European Space Agency, "Biomass: Report for mission selection," ESA Communication Production Office, SP-1324/1, 2012. [Online]. Available: https://earth.esa.int/web/guest/documentlibrary/browse-document-library/-/article/biomass-report-for-missionselection-an-earth-explorer-to-observe-forest-biomass

[3] F. J. Meyer and J. B. Nicoll, "Prediction, detection and correction of Faraday rotation in full-polarimetric L-band SAR data," *IEEE Trans.Geosci. Remote Sens.*, vol. 46, no. 10, pp. 3076–3086, Oct. 2008.

[4] Z. Li and Y. Zan, "Performance analysis of autofocus algorithms for compensating ionospheric dispersion effect on spaceborne low-frequency SAR focusing," *IEEE Geosci. Remote Sens. Lett.*, vol. 18, no. 2, pp. 331–335, Feb. 2021.

[5] J. S. Kim, K. P. Papathanassiou, R. Scheiber, and S. Quegan, "Correcting distortion of polarimetric SAR data induced by ionospheric scintillation," *IEEE Trans. Geosci. Remote Sens.*, vol. 53, no. 12, pp. 6319–6335, Dec. 2015.

[6] S. Quegan and M. R. Lomas, "The impact of system effects on estimates of Faraday rotation from synthetic aperture radar measurements," *IEEE Trans. Geosci. Remote Sens.*, vol. 53, no. 8, pp. 4284–4298, Aug. 2015.

[7] S. H. Bickel and R. H. T. Bates, "Effects of magneto-ionic propagation on the polarization scattering matrix," *Proc. IEEE*, vol. 53, no. 8, pp. 1089–1091, Aug. 1965.

[8] A. Freeman, "Calibration of linearly polarized polarimetric SAR data subject to Faraday rotation," *IEEE Trans. Geosci. Remote Sens.*, vol. 42, no. 8, pp. 1617–1624, Aug. 2004.

[9] J. Chen and S. Quegan, "Improved estimators of Faraday rotation in spaceborne polarimetric SAR data," *IEEE Geosci. Remote Sens. Lett.*, vol. 7, no. 4, pp. 846–850, Oct. 2010.

[10] L. Li, Y. Zhang, Z. Dong, and D. Liang, "New Faraday rotation estimators based on polarimetric covariance matrix," *IEEE Geosci. Remote Sens. Lett.*, vol. 11, no. 1, pp. 133–137, Jan. 2014.

[11] J. Li, Y. Ji, Y. Zhang, Q. Zhang, H. Huang, and Z. Dong, "Effects of polarimetric dispersion on future spaceborne P-band ultra-wideband SAR," *Electron. Lett.*, vol. 54, no. 22, pp. 1292–1294, Nov. 2018.

[12] D. Belcher, "Theoretical limits on SAR imposed by the ionosphere," *IET Radar, Sonar Navig.*, vol. 2, no. 6, pp. 435–448, Dec. 2008.

[13] H. Lijia, D. Chibiao, Q. Xiaolan, Z. Hongyi, and L. Liang, "Ionosphere estimation and correction for geosynchronous SAR based on point target

deviation between range sub-images," in *Proc. IEEE 13th Int. Conf. Signal Process.*, Nov. 2016, pp. 1886–1889.
[14] D. P. Belcher and N. C. Rogers, "Theory and simulation of ionospheric effects on synthetic aperture radar," *IET Radar Sonar Navig.,* vol. 3, no. 5, pp. 1–11, Oct. 2009.
[15] C. Hu, Y. Li, X. Dong, R. Wang, and D. Ao, "Performance analysis of L-band geosynchronous SAR imaging in the presence of ionospheric scintillation," *IEEE Trans. Geosci. Remote Sens.*, vol. 55, no. 1, pp. 159–172, Jan. 2017.
[16] Z. Li, S. Quegan, J. Chen, and N. C. Rogers, "Performance analysis of phase gradient autofocus for compensating ionospheric phase scintillation in BIOMASS P-Band SAR data," *IEEE Geosci. Remote Sens. Lett.*, vol. 12, no. 6, pp. 1367–1371, Jun. 2015.
[17] S. Quegan, J. Green, and R. Z. Schneider, "Quantifying and correcting ionospheric effects on P-band SAR images," in *Proc. IEEE Geosci. Remote Sens. Symp* ., Jul. 2008, pp. 541–544.
[18] Y. Ji, Z. Dong, Y. Zhang, Q. Zhang, L. Yu, and B. Qin, "Measuring ionospheric scintillation parameters from SAR images using phase gradient autofocus: A case study," *IEEE Trans. Geosci. Remote Sens.*, vol. 60, pp. 1–12, 2022, Art. no. 5200212, doi: 10.1109/TGRS.2020.3044657.
[19] L. Yu, Y. Zhang, Q. Zhang, Z. Dong, Y. Ji, and B. Qin, "A novel ionospheric scintillation mitigation method based on minimum-entropy autofocus in P-band SAR imaging," in *Proc. IEEE Int. Conf. Signal Image Process.*, Jul. 2019, pp. 198–202.
[20] L. Yu, Y. Zhang, Q. Zhang, Y. Ji, and Z. Dong, "Minimum-entropy autofocusing based on Re-PSO for ionospheric scintillation mitigation in P-band SAR imaging," *IEEE Access*, vol. 7, pp. 84580–84590, Jun. 2019.
[21] J. Li, J. Chen, P. Wang, and O. Loffeld, "A coarse-to-fine autofocus approach for very high-resolution airborne stripmap SAR imagery," *IEEE Trans. Geosci. Remote Sens.*, vol. 56, no. 7, pp. 3814–3829, Jul. 2018.
[22] L. Ran, R. Xie, Z. Liu, L. Zhang, T. Li, and J. Wang, "Simultaneous range and cross-range variant phase error estimation and compensation for highly squinted SAR imaging," *IEEE Trans. Geosci. Remote Sens.*, vol. 56, no. 8, pp. 4448–4463, Aug. 2018.
[23] H. L. Chan and T. S. Yeo, "Noniterative quality phase-gradient autofocus (QPGA) algorithm for spotlight SAR imagery," *IEEE Trans. Geosci. Remote Sens.*, vol. 36, no. 5, pp. 1531–1539, Sep. 1998.
[24] W. Ye, T. S. Yeo, and Z. Bao, "Weighted least-squares estimation of phase errors for SAR/ISAR autofocus," *IEEE Trans. Geosci. Remote Sens.*, vol. 37, no. 5, pp. 2487–2494, Sep. 1999.
[25] K. A. C. de Macedo, R. Scheiber, and A. Moreira, "An autofocus approach for residual motion errors with application to airborne repeat-pass SAR interferometry," in *Proc. IEEE Geosci. Remote Sens. Symp.*, Jul. 2007, pp. 4886–4889.
[26] C. S. Carrano, K. M. Groves, and R. G. Caton, "Simulating the impacts of ionospheric scintillation on L band SAR image formation," *Radio Sci.*, vol. 47, no. 4, pp. 1–14, Aug. 2012.
[27] J. A. Secan, *WBMOD Ionospheric Scintillation Model—An Abbreviated User's Guide (v. 15)*. Tucson, AZ, USA: North West Res. Inst., Aug. 2007.
[28] J. Wang and X. Liu, "SAR minimum-entropy autofocus using an adaptive-order polynomial model," *IEEE Geosci. Remote Sens. Lett.*, vol. 3, no. 4, pp. 512–516, Oct. 2006.

Hongcheng Zeng (Member, IEEE) was born in 1989. He received the Ph.D. degree in signal and information processing from Beihang University, Beijing, China, in 2016.

Since 2019, he has been an Assistant Professor with the School of Electronics and Information Engineering, Beihang University. From 2017 to 2018, he was a Visiting Researcher with the School of Mathematics and Statistics, University of Sheffield, Sheffield, U.K. He has published more than 20 journal and conference papers. His research interests include high-resolution spaceborne SAR image formation, passive radar signal processing, and moving target detection.

Wei Yang was born in 1983. He received the M.S. and Ph.D. degrees in signal and information processing from Beihang University (BUAA), Beijing, China, in 2008 and 2011, respectively.

From 2011 to 2013, he held a postdoctoral position at the School of Electronics and Information Engineering, BUAA. Since July 2013, he has been with the School of Electronics and Information Engineering, BUAA, as a Lecturer. From 2016 to 2017, he researched as a Visiting Researcher with the Department of Electronic and Electrical Engineering, University of Sheffield, Sheffield, U.K. Since 2018, he has been an Associate Professor with the School of Electronics and Information Engineering, BUAA. He has authored or coauthored more than 60 journal and conference publications. His research interests include moving target detection, high-resolution spaceborne SAR image formation, SAR image quality improvement, and 3-D imaging.

Pengbo Wang was born in 1979. He received the Ph.D. degree in information and communication engineering from Beihang University, Beijing, China, in 2007.

From 2007 to 2010, he held a Postdoctoral Position with the School of Electronics and Information Engineering, Beihang University. From 2014 to 2015, he was a Visiting Researcher with the Department of Electronic and Electrical Engineering, University of Sheffield, Sheffield, U.K. Since 2015, he has been an Associate Professor with the School of Electronics and Information Engineering, Beihang University. His research interests include high-resolution spaceborne synthetic aperture radar (SAR) image formation, novel techniques for spaceborne SAR systems, and multimodal remote sensing data fusion.

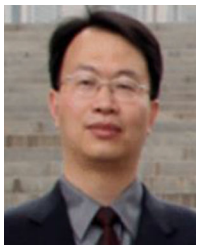

Jie Chen (Senior Member, IEEE) was born in 1973. He received the B.S. and Ph.D. degrees in information and communication engineering from Beihang University, Beijing, China, in 1996 and 2002, respectively.

Since 2004, he has been an Associate Professor with the School of Electronics and Information Engineering, Beihang University. From 2009 to 2010, he was a Visiting Researcher with the School of Mathematics and Statistics, University of Sheffield, Sheffield, U.K., working on ionospheric effects on low-frequency space radars that measure forest biomass and ionospheric electron densities. Since July 2011, he has been a Professor with the School of Electronics and Information Engineering, Beihang University. His research interests include multimodal remote sensing data fusion, and high-resolution spaceborne synthetic aperture radar (SAR) image formation and SAR image quality enhancement.